Dear authors,
thank you for taking all my remarks into account. I'm left with two minor issues, both on page 18.
* line 383: you always considered the year 2006 in your comparisons, and January and July 2006 in particular in Section 3.2. So, why are you comparing OMI version 3.0 with SSMIS for July 2007 here? Or is it a typo?
* lines 390-391: Why this inconsistency in filtering out pixels affected by rain between Fig. 6 and Table 3? Please give a reason for this approach.

Dear reviewer,

Thanks for your review.

For line 383, it is a typo. The year used should be 2006. Thanks for catching it. We have made the correction.

For line 390-391, SSMIS data have lower quality when there is precipitation. Thus, we have filtered out pixels with rain in both Figure 6 and Table 3. However, Figure 6 is dedicated to the comparison under "clear-sky" condition and Table 3 is for investigating the influence of different cloud fractions. We have therefore filtered out SSMIS pixels with cloud liquid water in Figure 6 and kept those pixels in Table 3. A comment about this has been added to the paper near line 391.

Regards,

from all authors

OMI Total Column Water Vapor Version 4 Validation and Applications

Huiqun Wang[1], Amir Hossein Souri[1], Gonzalo González Abad[1], Xiong Liu[1] and Kelly Chance[1]

[1]. Smithsonian Astrophysical Observatory, 60 Garden Street, Cambridge, Massachusetts 02138, USA

Correspondence to: Huiqun (Helen) Wang (hwang@cfa.harvard.edu)

Abstract

Total Column Water Vapor (TCWV) is important for the weather and climate. TCWV is derived from the Ozone Monitoring Instrument (OMI) visible spectra using the Version 4.0 retrieval algorithm developed at the Smithsonian Astrophysical Observatory. The algorithm uses a retrieval window between 432.0 and 466.5 nm and includes updates to reference spectra and water vapor profiles. The retrieval window optimization results from the trade-offs among competing factors.

The OMI product is characterized by comparing against commonly used reference datasets – Global Positioning System (GPS) network data over land and Special Sensor Microwave Imager / Sounder (SSMIS) data over the oceans. We examine how cloud fraction and cloud top pressure affect the comparisons. The results lead us to recommend filtering OMI data with cloud fraction less than f = 0.05 - 0.25 and cloud top pressure > 750 mb (or stricter), in addition to the data quality flag, fitting RMS and TCWV range check. Over land, for f = 0.05, the overall mean of (OMI-GPS) is 0.32 mm with a standard deviation (σ) of 5.2 mm, the smallest bias occurs when TCWV = 10 – 20 mm, and the best regression line corresponds to f = 0.25; Over the oceans, for f = 0.05, the overall mean of (OMI-SSMIS) is 0.4 mm (1.1 mm) with σ = 6.5 mm (6.8 mm) for January (July), the smallest bias occurs when TCWV = 20 – 30 mm, and best regression line corresponds to f = 0.15. For both land and the oceans, the difference between OMI and the reference datasets is relatively large when TCWV is less than 10 mm. The bias for Version 4.0 OMI TCWV is much smaller than that for Version 3.0.

As test applications of the Version 4.0 OMI TCWV over a range of spatial and temporal scales, we find prominent signals of the patterns associated with El Niño and La Niña, the high

humidity associated with a corn sweat event and the strong moisture band of an atmospheric river (AR). A data assimilation experiment demonstrates that the OMI data can help improve the Weather Research and Forecasting model (WRF)'s skill at simulating the structure and intensity of the AR and the precipitation at the AR landfall.

1 Introduction

Water vapor is of profound importance for weather and climate. Through condensation, it forms clouds that modify albedo, affect radiation and interact with particulate matter. In addition, latent heat released from water vapor condensation can influence atmospheric energy budget and circulation. Water vapor is the most abundant greenhouse gas, accounting for ~50% of the greenhouse effect (Schmidt et al., 2010). Thus, monitoring the spatial and temporal distributions of water vapor is crucial for understanding water-vapor related processes.

Water vapor has been measured using a variety of in situ and remote sensing techniques from the ground, air and space. Satellite data provide global perspective and are indispensable for constraining reanalysis products (Dee et al., 2011; Gelaro et al., 2017). The current satellite water vapor datasets are evaluated through the Global Energy and Water cycle Exchanges (GEWEX) Water Vapor Assessment program (Schröder et al., 2019). These datasets are derived from visible, near infrared (NIR), Infrared (IR), microwave and Global Positioning System (GPS) measurements. Each dataset has its own characteristics and contributes to the understanding of water vapor in its own way. For example, microwave data are useful for both clear-sky and cloudy-sky conditions, but are best suited for non-precipitating ice-free oceans due to the complications associated with land surface emissivity; NIR data are best suited for the land, as the surface albedo is low over the oceans; IR data are available over all surface types, but are strongly influenced by clouds and less sensitive to the planetary boundary layer; visible data are sensitive to the boundary layer over both land and the oceans, but are complicated by uncertainties in clouds and aerosols (Wagner et al., 2013).

Total Column Water Vapor (TCWV, also called Integrated Water Vapor - IWV, or Precipitable Water Vapor - PWV) can be retrieved from the 7ν water vapor vibrational polyad band (around 442 nm) despite the weak absorption (Wagner et al., 2013). This made it possible to derive TCWV from instruments measuring in the blue wavelength range. Since water vapor is a weak absorber here, saturation of spectral lines is not of concern (Noël et al., 1999). Moreover, the similarity between the land and ocean surface albedo in the blue wavelength range suggests a roughly uniform sensitivity of the measurement over the globe (Wagner et al., 2013). However, weaker absorption tends to result in larger relative uncertainties, especially for low TCWV amount.

Using the visible spectra measured by the Ozone Monitoring Instrument (OMI), Wang et al. (2014) retrieved Version 1.0 TCWV from 430 – 480 nm and publically released the data on the Aura Validation Data Center (AVDC, https://avdc.gsfc.nasa.gov). Wang et al. (2016) found that the Version 1.0 data generally agree with ground-based GPS data over land but are significantly lower than the microwave observations over the oceans. They found that using a narrower retrieval window (427.7 – 465 nm) in Version 2.1 could improve the data over the oceans without adversely affecting the results over land much. However, the Version 2.1 data were only generated for a few test months and not released to the public. An interim Version 3.0 OMI TCWV product was available at AVDC. Compared with Version 2.1, Version 3.0 uses the reference spectrum for water vapor from the latest HITRAN database (Gordon et al., 2016) and that for liquid water from Mason et al. (2016), as well as the newest cloud product (Veefkind et al., 2016). The Version 3.0 retrieval window (427.0 – 467.0 nm) is adjusted from that for Version 2 within 2 nm on each end based on fitting uncertainty for a randomly selected test orbit.

This paper focuses on Version 4.0 OMI TCWV which has replaced Version 3.0 on AVDC. We present the Version 4.0 retrieval algorithm which incorporates a more vigorous systematic optimization for the retrieval window and miscellaneous updates. We characterize the performance of the Version 4.0 dataset by comparing with well-established references, such as the GPS network data and the Special Sensor Microwave Imager / Sounder (SSMIS) observations. We also assess the performance of Version 4.0 against that of Version 3.0. To provide practical guide to users of the new data, we investigate the influence of cloud fraction and cloud top pressure on the comparisons. Based on the results, data filtering criteria are recommended. As an additional check on the Version 4.0 product, we show test applications of the data to a range of spatial and temporal scales, including El Niño / La Niña, a corn sweat event and an atmospheric river (AR) event. For the first time, a data assimilation experiment for the AR event demonstrates that the OMI TCWV data can provide useful constraint for weather prediction.

2 Retrieval Algorithm

OMI on board the Aura spacecraft is a UV/Visible imaging spectrometer (Levelt et al., 2006). It has been making daily global observations at a nominal 13×24 km nadir resolution from a 1:30 PM equator crossing time polar orbit since October 2004. The UV-Visible channel of OMI covers 350-500 nm at a spectral resolution of about 0.5 nm.

TCWV is derived from the OMI visible spectrum using a commonly used two-step approach. First, the Slant Column Density (SCD, molecules/cm^2) is retrieved from a spectral fitting algorithm. Then, the Vertical Column Density (VCD, molecules/cm^2) is calculated from the ratio of SCD and Air Mass Factor (AMF) (Palmer et al., 2001). VCD can be converted to TCWV using 10^{23} molecules/cm^2 = 29.89 mm. The details of the two-step procedure can be found in González Abad et al. (2015). The specifics of Version 4.0 are discussed below.

The Version 4.0 spectral fitting parameters are summarized in Table 1. In the nonlinear least square fitting, we consider wavelength shift, under-sampling, closure polynomials (3rd order multiplicative and additive), reference spectroscopic spectra of water vapor, interfering molecules (O_3, NO_2, O_4, liquid water, $C_2H_2O_2$ and IO) and Raman scattering (the Ring effect, vibrational Raman scattering of air and the water Ring effect). In comparison with previous versions, Version 4.0 no longer fits common mode (i.e. the mean of the fitting residual, González Abad et al., 2015). It turns out that the common mode for land is different than that for ocean (Wang et al., 2014). Previous retrievals derive a common mode for each orbit swath using the pixels in the low latitudes which often includes both land and ocean scenes. Thus, the derived common mode depends on the proportion of land versus ocean pixels of the spacecraft orbit and is not universally suitable for all the pixels of the swath. Statistics for Orbit 10423 show that although the mean of SCD differs little between the retrievals with and without common mode in the fitting (0.1 mm), the standard deviation of SCD between them can be significant (1.7 mm). Most of the settings in Table 1 are shared between Version 3.0 and 4.0, except that Version 3.0 uses HITRAN 2016 (Gordon et al., 2016) as the water vapor reference spectrum, includes common mode in the fitting, but does not consider vibrational Raman scattering of air (Lampel et al., 2015a). We revert to the HITRAN 2008 water vapor spectrum (Rothman et al., 2009) in Version 4.0 because validation results show that it leads to better agreements with the GPS and SSMIS TCWV data (Section 3). We did not apply the correction of Lampel et al. (2015b) to the

HITRAN 2008 water vapor spectrum. It is recently found that HITRAN 2016 is adversely affected by an issue with line broadening for water vapor in the blue wavelength range and improvements are being made for the next HITRAN release (the HITRAN group, personal communication).

Table 1. Parameters used in Version 4.0 spectral fitting for OMI total column water vapor.

Wavelength shift	Solar reference spectrum	Dobber et al. (2008)
Target	H_2O	288K, Rothman et al. (2009)
Interference molecules	O_3	228K, Brion et al. (1993)
	NO_2	220K, Vandaele et al. (1998)
	O_4	293K, Thalman and Volkamer (2013)
	Liquid water	Mason et al. (2016)
	$C_2H_2O_2$	296K, Volkamer et al. (2005)
	IO	298K, Spietz et al. (2005)
Raman scattering	Ring effect	Chance and Spurr (1997)
	Water Ring	Chance and Spurr (1997)
	Air Vibrational Raman	Lampel et al. (2015a)
Other	Additive polynomial	3^{rd} order
	Multiplicative polynomial	3^{rd} order
	Under-sampling	Chance et al. (2005)

To optimize the retrieval window, we randomly selected OMI Orbit number 10426 (on July 1, 2006) to examine the effect of varying the starting and ending wavelengths around the 7ν water vapor absorption band. The orbit swath contains 60×1644 ground pixels and covers parts of Australia, the Pacific, China and other areas. We systematically adjust the starting wavelength within 426.0-435.0 nm and the ending wavelength within 460.0-468.5 nm, both at 0.5 nm steps.

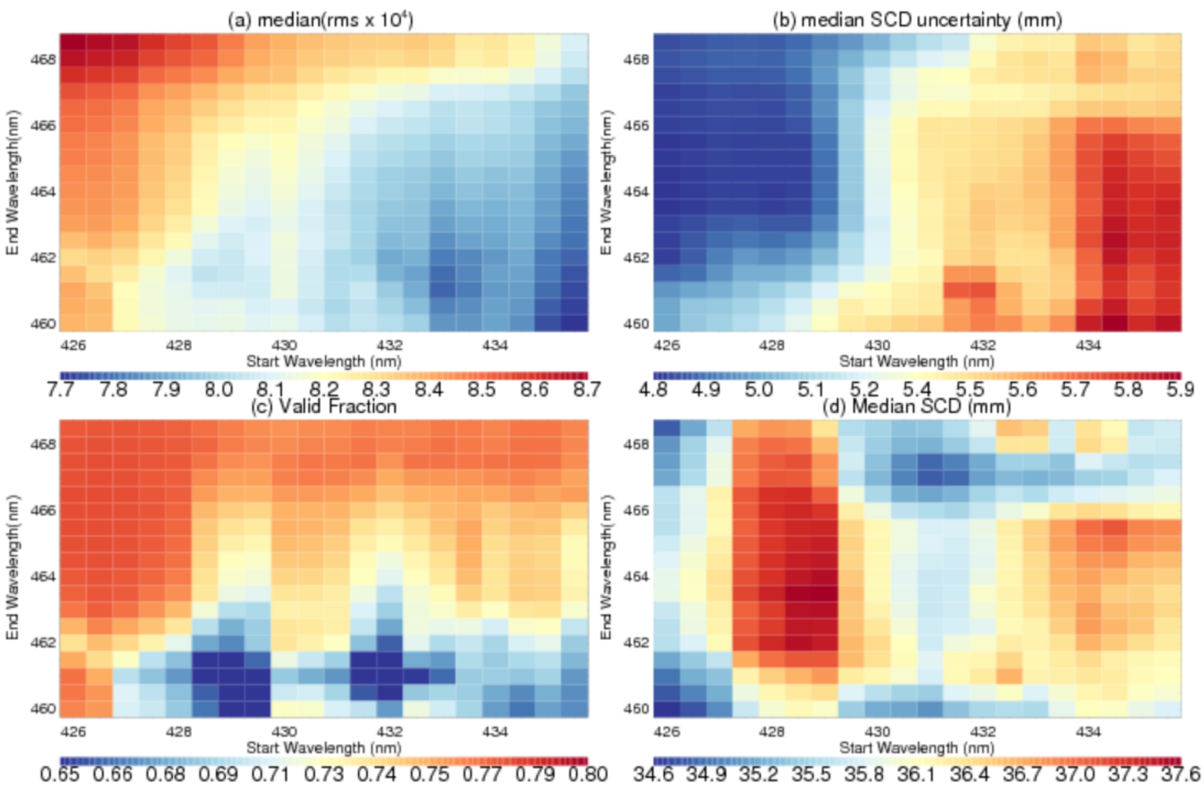

Figure 1. Sensitivity of the retrieval to the start and end wavelengths (nm) of the retrieval window for OMI Orbit number 10426. (a) Median of fitting RMS×10^4; (b) median of water vapor SCD fitting uncertainty in mm; (c) valid fraction for retrievals; (d) median SCD in mm.

In previous versions, the fitting window is selected based on the fitting uncertainty (Wang et al., 2014, 2016). For Version 4.0, we consider the following four factors. (1) Figure 1a shows that the median of the fitting Root Mean Squared error (RMS) is smaller toward the lower right corner of the domain (i.e., longer start wavelength and shorter end wavelength); (2) Figure 1b shows that the medium fitting uncertainty of water vapor SCD decreases toward the upper left corner; (3) Figure 1c shows that the fraction of valid retrievals for the orbit generally increases toward the upper part of the domain. Valid retrievals here refer to those that pass the main data quality check (MDQFL = 0) and have positive SCDs. The main data quality check ensures that the fitting has converged, the SCD is < 5×10^{23} molecules/cm^2 (149.45 mm) and within 2σ of the fitting uncertainty. The SCD threshold here is meant to filter out large outliers. For reference, the largest TCWV of the GPS and SSMIS datasets used in Section 3 is about 75 mm. At low latitudes where TCWV is large, more than 90% of the OMI AMFs are between 0.5 and 2.0; (4) The length of the retrieval window increases with the difference between the end and start wavelengths. The general patterns exhibited by Orbit number 10426 in Figure 1 also hold for Orbit number 10423 which cuts across the Pacific near the dateline.

Ideally, we would like to have small fitting RMS to reduce the residual's amplitude and structure, a small fitting uncertainty to reduce error, a large fraction of valid data to increase data volume and a long retrieval window to include more information into the fitting. However, these criteria cannot be met simultaneously. As a compromise, we select the wavelength interval between 432.0 nm and 466.5 nm as the retrieval window for Version 4.0. For Orbit number 10426, this leads to a median fitting RMS of 8.1×10^{-4}, a median SCD uncertainty of 5.4 mm, a valid fraction of 0.75 and a window length of 34.5 nm (Figure 1). Figure 1d shows that the median SCD for Orbit number 10426 varies between 34.6 mm and 37.6 mm. This 3 mm difference corresponds to an 8% variation and exhibits a complex pattern within the domain. The Version 4.0 retrieval window leads to a median SCD of 35.5 mm for Orbit number 10426 which is near the beginning of the middle third of the SCD range. The ratio between the median SCD uncertainty and the median SCD (i.e., the relative SCD uncertainty) is about 0.15. Note that this value is for the whole orbit which includes a wide range of SCDs. As shown in Supplementary Figure 1, the relative SCD uncertainty is >1.2 for SCD = 0 – 10 mm, drops to about 0.4 for SCD = 10 – 20 mm, and to about 0.1 for SCD > 40 mm.

The AMF is calculated by convolving scattering weights with the shape of water vapor vertical profile (González Abad et al., 2015). The scattering weight is interpolated from the same look-up table as that used in Wang et al. (2016). The scene specific information used in the AMF calculation is listed in Table 2. By propagating typical errors for surface albedo (15%), cloud fraction (10%) and cloud top pressure (15%), we find that the AMF error due to scattering weight for a typical orbit (number 10426) is mostly < 3%, though for cloudy pixels, the error can be 15% or more. Version 4.0 uses the 0.5°×0.667° monthly mean MERRA-2 water vapor profile (Gelaro et al., 2017) for the month and year corresponding to the retrieval, while previous versions used the monthly mean of 2007 for all years. To evaluate the error associated with gas profiles, we compare the TCWV calculated using the daily MERRA-2 profile against that calculated using the monthly MERRA-2 profile for July 2006 (for TCWV within the 0 – 75 mm range). Results show that (TCWV(daily) – TCWV(monthly)) has a mean (median) of 0.3 mm (0 mm) with a standard deviation of 5.0 mm. When comparing the TCWV calculated using the daily MERRA-2 profile against that calculated using the daily ERA-Interim profile for July

2006, we find that (TCWV(MERRA-2) – TCWV(ERA-Interim)) has a mean (median) of -0.1 mm (0 mm) with a standard deviation of 2.8 mm. Thus, gas profiles can introduce substantial scatter to the retrieved TCWV. AMF is highly sensitive to clouds (Wang et al., 2014; Vasilkov et al., 2017). Version 4.0 uses the cloud information from Veefkind et al. (2016). The primary difference with the Acarreta et al. (2004) cloud product used in Version 1.0 and 2.1 is in the cloud top pressure for cloud fraction $f < 0.3$. In addition to the factors in Table 2, aerosol and surface bi-directional reflectance distribution function (BRDF) influence the AMF (Lorente et al., 2017; Vasilkov et al., 2017), but have not been considered in the retrieval yet.

Table 2. Parameters used in AMF calculation

Solar Zenith Angle	OMI L1B data
View Zenith Angle	
Relative Azimuth Angle	
Surface Albedo	OMLER (Lambert equivalent reflectance) Kleipool, et al. (2008)
Cloud fraction	OMCLDO2 (derived from O_2-O_2) Veefkind et al. (2016)
Cloud top pressure	
Surface pressure	MERRA-2 monthly data (0.5°×0.667°), Gelaro et al. (2017)
Water vapor profile	

3 Validation

To validate the Version 4.0 OMI TCWV data, we compare them against two commonly used reference datasets – a GPS network dataset for land and a microwave dataset for the oceans.

3.1 OMI and GPS over land

To assess the Version 4.0 OMI TCWV over land, we compare against the GPS network data downloaded from NCAR (rda.ucar.edu/datasets/ds721.1). The GPS data are composed of 2-hourly TCWV at International GNSS Service (IGS), SuomiNet and GEONET stations, and have an estimated error of < 1.5 mm (Wang et al., 2007; Ning et al., 2016). The subset of IGS-SuomiNet data for the whole year of 2006 is used in this paper. The geographical distribution of the stations can be found in Wang et al. (2016). Most of the stations are concentrated in North America and Europe, fewer are scattered on other continents.

OMI TCWV data are filtered using the following criteria. The stripes in Level 2 swaths due to systematic instrument error are removed using the SCD scaling procedure described in Wang et al. (2016). The pixels affected by OMI's row anomaly are filtered out (projects.knmi.nl/omi/research/product/rowanomaly-background.php), as well as negative or extremely large (i.e., TCWV > 75 mm) values. For the clear-sky comparison in Figure 3, we require cloud fraction < 5% and cloud top pressure > 750 mb, in addition to MDQFL = 0 and fitting RMS < 0.001. The cloud fraction and cloud top pressure are from the OMCLDO2 cloud product (Veefkind et al., 2016) and are included in the Level 2 OMI product for ease of data filtering. On a typical day (July 1, 2006), among the OMI data that pass the MDQFL and TCWV range test, cloud fraction < 0.05 accounts for 35% of the data, cloud top pressure > 750 mb accounts for 53% of the data and RMS < 0.001 accounts for 72% of the data.

To co-locate GPS and OMI data, we select the GPS data observed between 1200 LT and 1500LT. This 3-hour local time range covers the OMI overpass time. We average the qualified OMI data within 0.25° longitude × 0.25° latitude of the GPS stations for each day. To minimize the influence of local topography (e.g., mountain peaks, river valleys), if a station's elevation is more than 250 m different than the mean elevation within the corresponding 0.25°×0.25° grid square, then it is excluded from the analysis. The 0.25°×0.25° topography was downloaded from www.temis.nl/data/topo/dem2grid.html. The comparison between OMI and GPS is made for TCWV within the range of 0 – 75 mm as the largest TCWV for the GPS data is about 75 mm. The co-locating procedure leads to about 11,000 co-located data points for the entire year of 2006.

Figure 2 shows the comparison between the resulting co-located GPS and Version 4 OMI TCWV. The top panel shows the histogram of OMI-GPS (in 0.5 mm bins). The bin from -0.5 to 0.0 mm corresponds to the peak of the distribution. The overall mean (median) of OMI-GPS is 0.32 mm (0.35 mm), with a standard deviation of 5.2 mm. The mean (median) absolute error is 3.9 mm (3.0 mm).

The bottom panel of Figure 2 shows the joint distribution of the co-located GPS and Version 4.0 OMI data. The count for each 0.5 mm bin is normalized by the maximum of all bins. About 34% of the data have TCWV < 10 mm, 72% have TCWV < 20 mm and 90% have TCWV < 30 mm. There is a general linear correlation between GPS and OMI data, with a correlation coefficient of r = 0.87 (R^2 = 0.76). The linear regression line (OMI = 2.22 + 0.88 * GPS, where OMI and GPS TCWV are in mm) has a significant positive intercept and a slope that is less than one. This indicates a positive bias of OMI against GPS for small TCWV and a negative bias for large TCWV. Indeed, as indicated at the top of the panel, the mean of OMI-GPS for each 10 mm GPS TCWV bin decreases from 1.7 mm for TCWV = 0 – 10 mm to -2.3 mm for TCWV = 40 – 50 mm, though the fraction of data for TCWV > 40 mm is < 3%. The corresponding standard deviation (σ) increases from 3.5 mm to 7.9 mm. The minimum bias of 0.2 mm occurs for TCWV in the 10 – 20 mm bin. The large positive bias of the 0 – 10 mm bin (as compared with the TCWV of the bin) has significant adverse effect on the regression line. For TCWV > 10 mm, the regression line (OMI = 1.51 + 0.91 × GPS) is better.

In comparison, although Version 3.0 OMI is similarly correlated with GPS (correlation coefficient r = 0.86), it has a much larger positive bias of 2.8 mm (with a standard deviation of 5.5 mm). The large bias is attributed to the much larger SCD of Version 3.0 (Supplementary Figure 2b), as the AMFs of both versions roughly follow the 1:1 line (Supplementary Figure 2a). Sensitivity tests show that the larger Version 3.0 SCD is primary due to the water vapor reference spectrum. If the water vapor reference spectrum in Version 4.0 is replaced with that of Version 3.0 (Test 1), then the median SCD increases by about 4.5 mm for Orbit 10423 (Supplementary Figure 2c). Modifying the retrieval window for Version 3.0 cannot sufficiently reduce the retrieved SCD, therefore cannot make significantly better agreement with the reference TCWV data. As Version 4.0 shows better performance, this paper focuses on characterizing Version 4.0 to provide useful information to potential users. In subsequent discussions, OMI data refer to Version 4.0 unless specified otherwise.

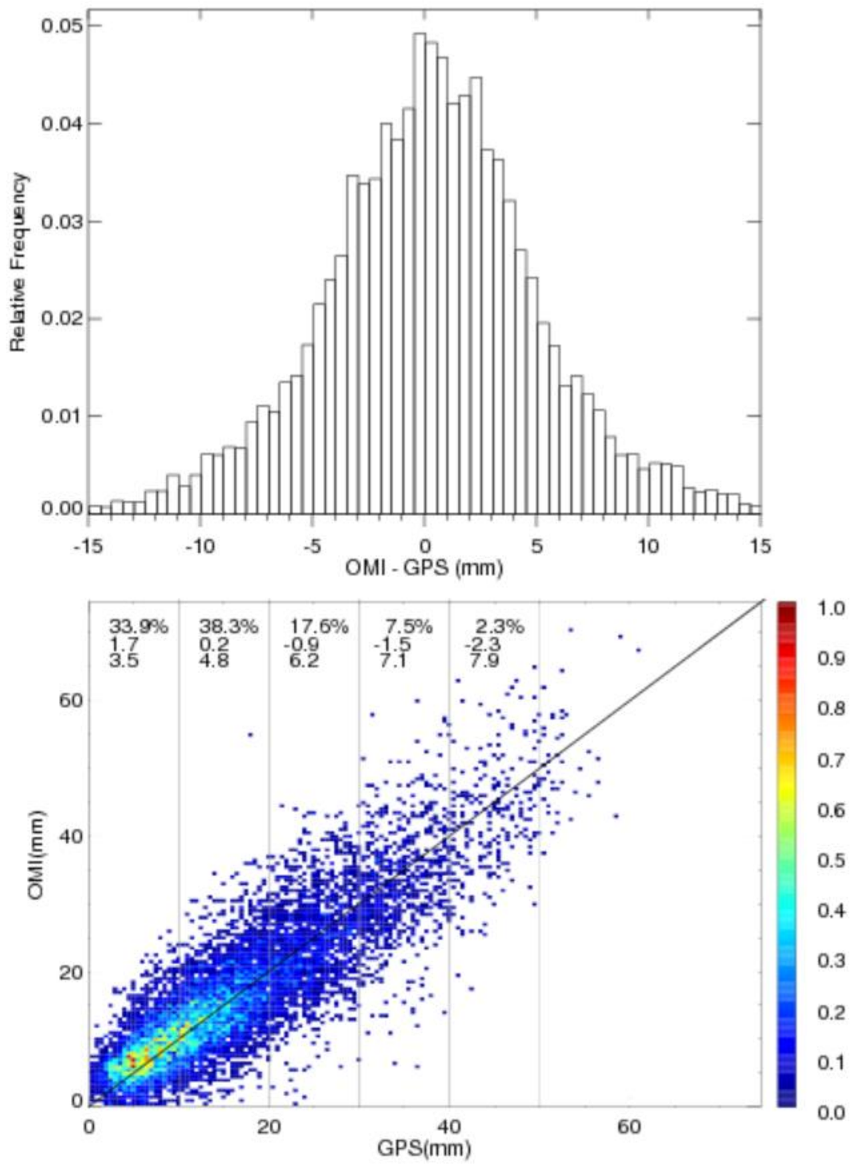

Figure 2. Comparison between co-located GPS and OMI TCWV (mm) for all days in 2006. The data filtering criteria include cloud fraction < 5%, cloud top pressure > 750 mb, and others discussed in the text. (Top) Relative frequency of occurrence for OMI-GPS (mm). (Bottom) Normalized joint distribution of GPS versus OMI TCWV (mm). The three lines of text from top to bottom indicate the percentage of data points (1st), the mean of OMI-GPS in mm (2nd), and the standard deviation of OMI-GPS in mm (3rd) for each 10 mm GPS TCWV, respectively. The 1:1 is plotted for reference.

OMI TCWV retrieval is highly sensitive to clouds (Wang et al., 2014). In Figure 3, we examine the effect of OMI cloud fraction threshold (f) on the comparison while keeping other data filtering criteria the same as those for Figure 2 (i.e., cloud fraction < f, cloud top pressure < 750 mb, MDQFL = 0, fitting RMS < 0.001 and 0 < TCWV<75 mm). From f = 0.05 to f = 0.55, the number of co-located data pairs (N) more than triples, the mean of OMI-GPS increases from 0.32 mm to 1.66 mm, the standard deviation of OMI-GPS increases from 5.2 mm to 6.1 mm. The linear correlation coefficient (r) increases from r = 0.87 at f = 0.05 to r ~ 0.90 at f = 0.15, then levels off for larger cloud fraction thresholds. It should be noted that the error in cloud top pressure decreases with cloud fraction in the OMCLDO2 product (Veefkind et al., 2016). As a result, f = 0.05 corresponds to the largest uncertainty in cloud top pressure, and the error will propagate into OMI TCWV through AMF, leading to smaller correlation coefficient than those for larger f values.

In addition, as shown by the GPS versus OMI joint distributions for different cloud fraction thresholds in Figure 4, the f ≥ 0.15 cases have larger effective dynamical ranges which tend to favor better correlations. For example, there is a larger fraction of data pairs with TCWV > 30 mm for f = 0.15 than for f = 0.05. The regression line for f = 0.15 (OMI = 1.26 + 0.96 * GPS) shows an apparent improvement over that for f = 0.05 (OMI = 2.22 + 0.88*GPS). The best regression line is arguably that for f = 0.25 (OMI = 1.16 + 0.99*GPS) or f = 0.35 (OMI = 1.19 + 1.00*GPS), though the mean bias and scatter are larger than those for f < 0.25 (Figure 4).

In brief, f = 0.05 leads to the lowest overall bias and scatter of the co-located data; f = 0.15 doubles the number of co-located data pairs and leads to the largest improvement in the correlation coefficient; f = 0.25 (or 0.35) leads to the best linear regression line; the bias and standard deviation increase with cloud fraction threshold. Hence, cloud fraction thresholds in the range of f = 0.05 – 0.25 seems reasonable for filtering OMI TCWV, depending on applications.

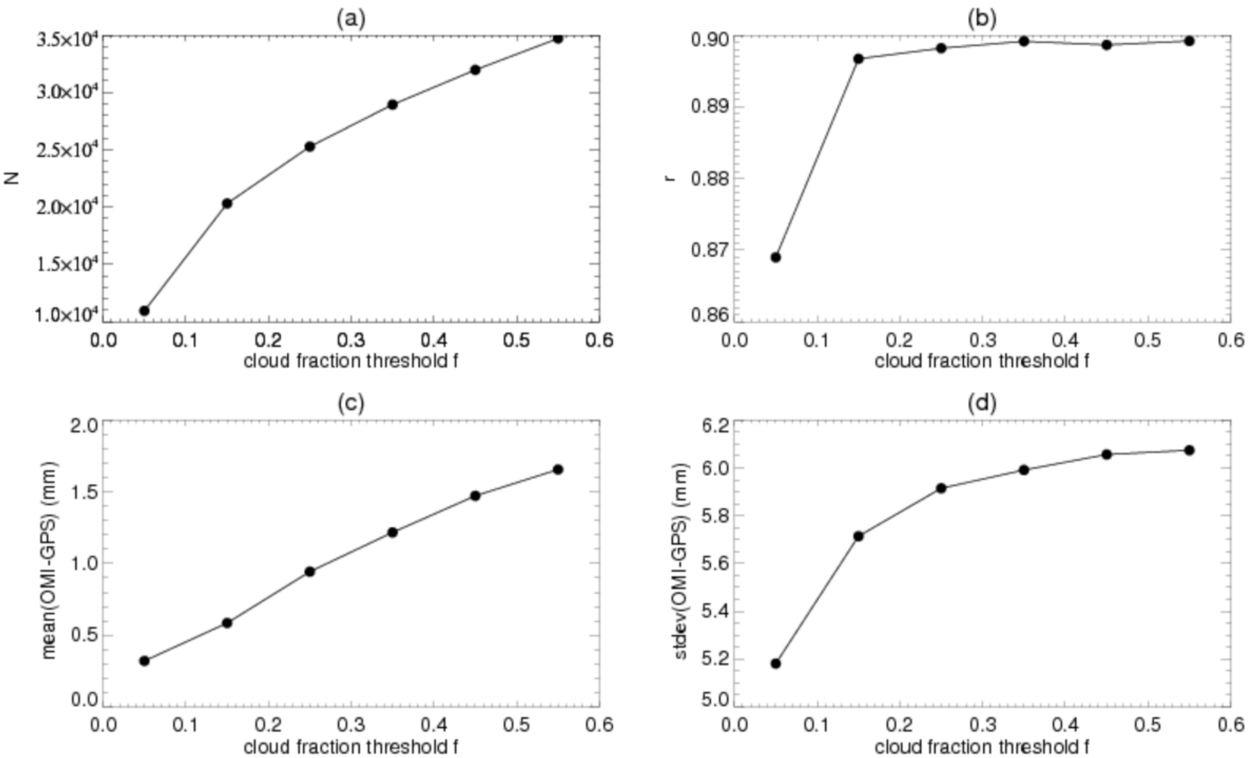

Figure 3. Dependence of various parameters on the cloud fraction threshold (f) used for filtering OMI data. Other filtering criteria remain the same as those for Figure 2. The parameters are (a) number of co-located OMI and GPS data pairs; (b) linear correlation coefficient between OMI and GPS TCWV; (c) mean of OMI-GPS in mm; (d) standard deviation of OMI-GPS in mm. Results are derived from the co-located Version 4.0 OMI and GPS data for the whole year of 2006.

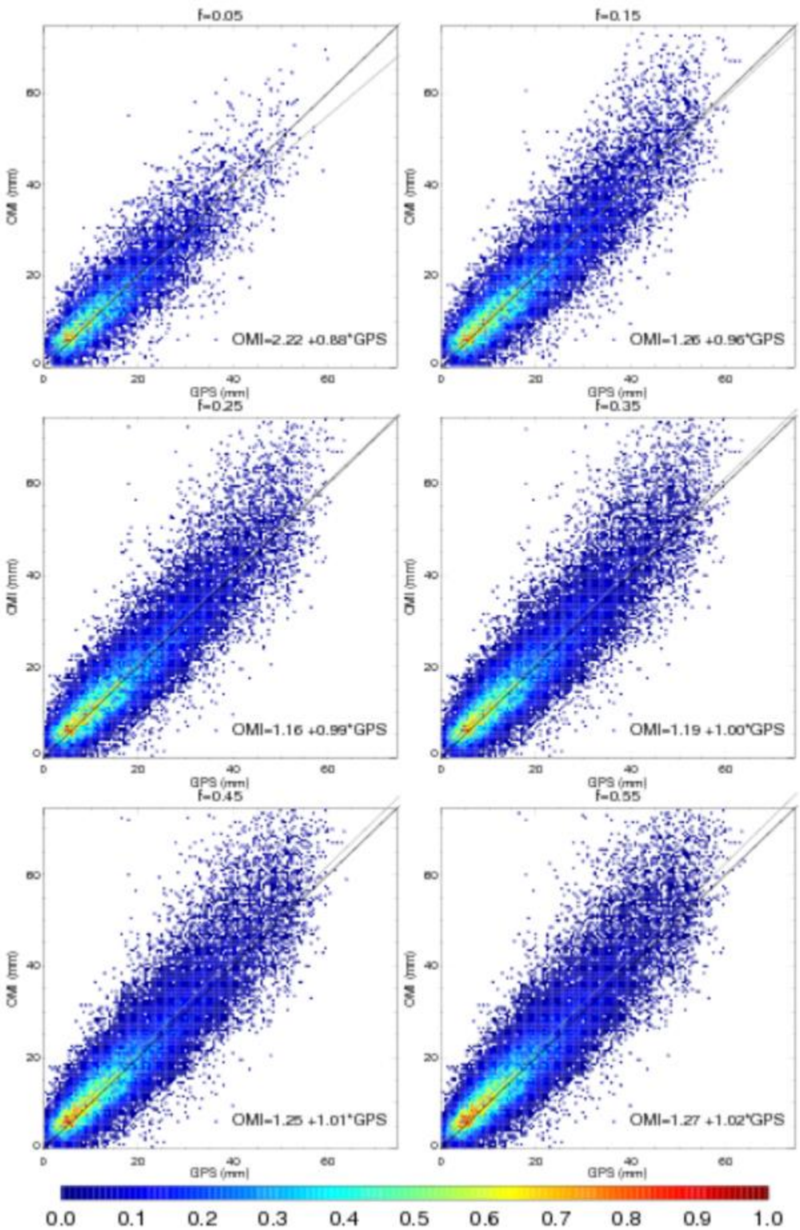

Figure 4. Normalized joint distributions of GPS versus Version 4.0 OMI TCWV for different cloud fraction thresholds. Results are derived from the co-located data pairs for 2006. The OMI data filtering criteria are the same as those for Figure 3. In each panel, the 1:1 line is plotted in black, the linear regression line is plotted in gray and indicated by the formula in the lower right corner.

To further characterize the effect of cloud fraction threshold on the comparison between GPS and OMI, in Figure 5, we examine the mean and standard deviation (σ) of OMI-GPS for each 10 mm GPS TCWV bin. The results are derived from the same sets of co-located GPS and OMI data as those used in Figure 3 and Figure 4. The filled symbols are for the cases where the number of GPS and OMI data pairs within the corresponding TCWV bin is > 1% of the total number of data pairs, and the open symbols are for < 1%. As the filled symbols represent better statistics, we will focus on them below.

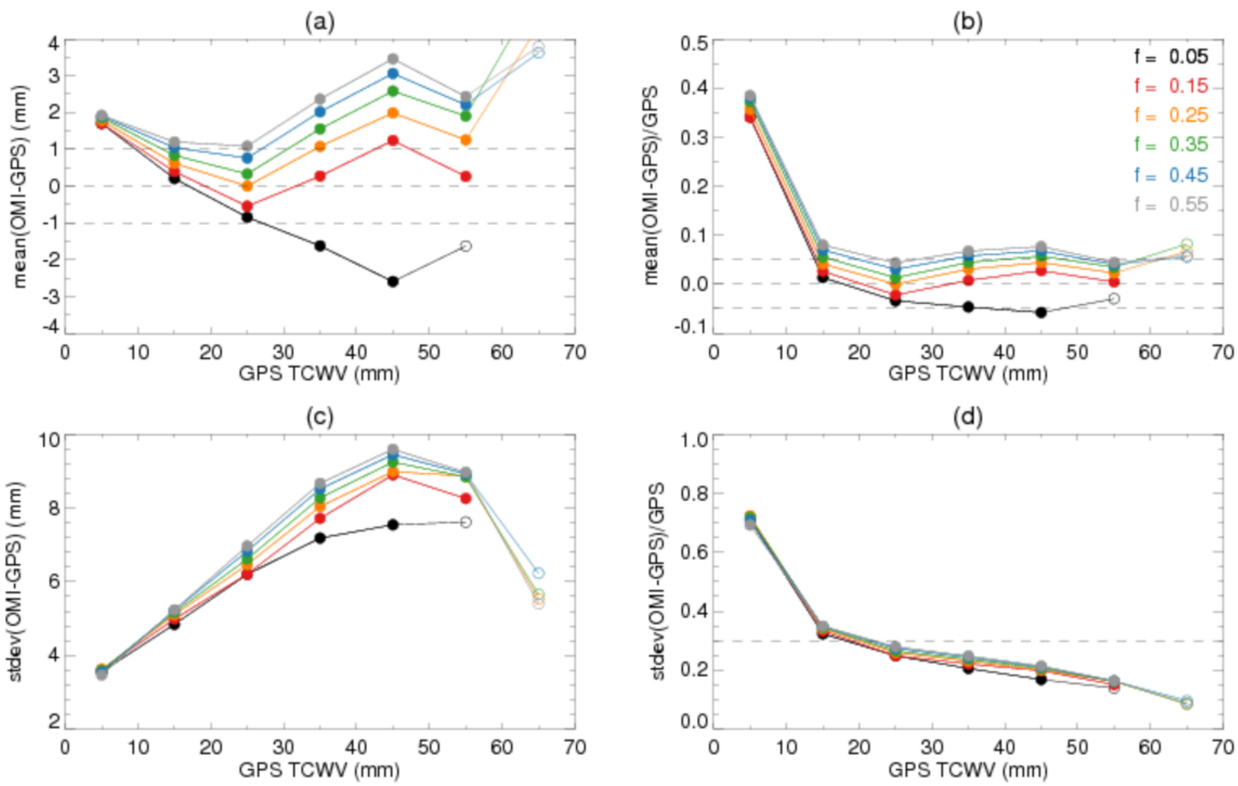

Figure 5. Parameters for each 10 mm TCWV bin. Curves with different colors are for different cloud fraction thresholds f as indicated in Panel (b). The OMI filtering criteria remain the same as those for Figure 3 and 4. Symbols are filled if the fraction of data pairs within the TCWV interval is > 1% of all the available data pairs and are open otherwise. The parameters are (a) mean of OMI-GPS in mm, (b) relative bias defined as mean(OMI-GPS)/GPS, (c) standard deviation (σ) of OMI-GPS in mm, and (d) relative scatter defined as σ/GPS. Results are for all days in 2006. Dashed lines are meant to facilitate visualization.

Figure 5(a) shows that the means of OMI-GPS vary between ±4 mm following “V”-shaped curves whose minima occur in the TCWV = 20 – 30 mm bin except for f = 0.05. The curves shift upward with increasing cloud fraction thresholds, suggesting that OMI cloudy-sky TCWV is generally larger than OMI clear-sky TCWV. Other things being equal, cloud formation indicates water vapor saturation and therefore a larger amount of TCWV than that under clear-sky condition. The smallest absolute bias for 10 < TCWV < 20 mm occurs at f = 0.05, that for 20 < TCWV < 30 mm occurs at f = 0.25, and that for 30 < TCWV < 40 mm occurs at f = 0.15. The f = 0.15 and f = 0.25 curves show the best overall performance according to Figure 5(a) as they are within 1 mm of zero for 10<TCWV<40 mm, while other curves come within 1 mm of zero in narrower TCWV ranges. Figure 5(b) shows the relative bias which is defined as the mean of (OMI-GPS)/GPS. The relative biases decrease sharply from ~40% to ~5% as GPS TCWV increases from the TCWV = 0 – 10 mm bin to the TCWV = 10 – 20 mm bin, and generally stay less than ~5 – 10 % for larger TCWV values. Figure 5(c) shows that σ increases from ~3.5 mm for TCWV = 0 - 10 mm to ~9.5 mm for TCWV = 40 - 50 mm (the percentage of data with TCWV > 50 mm is very small). In most cases, larger cloud fraction thresholds correspond to larger σ values. This is consistent with the larger dynamical range (due to a larger fraction of data with high TCWV) for larger cloud fraction threshold (Figure 4). In fact, the relative scatter, defined as the mean of σ/TCWV, shows little difference among the f values (Figure 5d). The relative scatter decreases with TCWV, with the sharpest decrease from ~0.7 to ~0.3 between TCWV = 0 – 10 mm and TCWV = 10 – 20 mm (Figure 5d). The relative scatter continues to decrease for larger TCWV and the overall scatter is about 20%.

In short, Version 4.0 OMI agrees with GPS within 1 mm for 10<TCWV<40 mm when f = 0.15 and f = 0.25 are used; when f = 0.05 is used, the bias and scatter are the smallest for 10<TCWV<20 mm; but, for TCWV < 10 mm, OMI TCWV is too high and has large relative scatter. The latter is expected from the low signal-to-noise ratio when TCWV < 10 mm in the OMI retrieval.

3.2 OMI and SSMIS over ocean

To evaluate Version 4.0 OMI TCWV over the oceans, we compare against the microwave TCWV data from SSMIS on board the Defense Meteorological Satellite Program (DMSP)'s F16 satellite. The SSMIS data are derived by Remote Sensing Systems (RSS) using their Version 7 algorithm (www.remss.com) and have a retrieval accuracy of better than 1 mm (Wentz, 1997; Mears et al., 2015). For clear-sky comparison, we use the daily 0.25°×0.25° SSMIS data for January and July 2006 and filter out the pixels affected by rain and cloud liquid water. Diedrich et al. (2016) found that the diurnal cycle in TCWV is generally within 1% to 5% of the daily mean, with a minimum between 0600 LT and 1000 LT and a maximum between 1600 LT and 2000 LT. To reduce the influence of diurnal cycle, we average the SSMIS data for the ascending and descending orbits of F16 (~2000 LT and 0800 LT in 2006).

We generate daily 0.25°×0.25° Level 3 OMI TCWV from the de-striped Level 2 OMI swaths, with the requirement that MDQFL = 0, fitting RMS < 0.001, 0<TCWV<75 mm, cloud fraction < 0.05, and cloud top pressure > 750 mb. There are typically 15 Level 2 swaths per day. The gridding program uses a tessellation method that weighs the contribution of a Level 2 data point by its area within the Level 3 grid square and its spectrum fitting uncertainty (Wang et al., 2014, 2016). The filtered daily Level 3 SSMIS and OMI data are compared for each month. We find 548,223 and 847,678 co-located data pairs for January and July 2006, respectively.

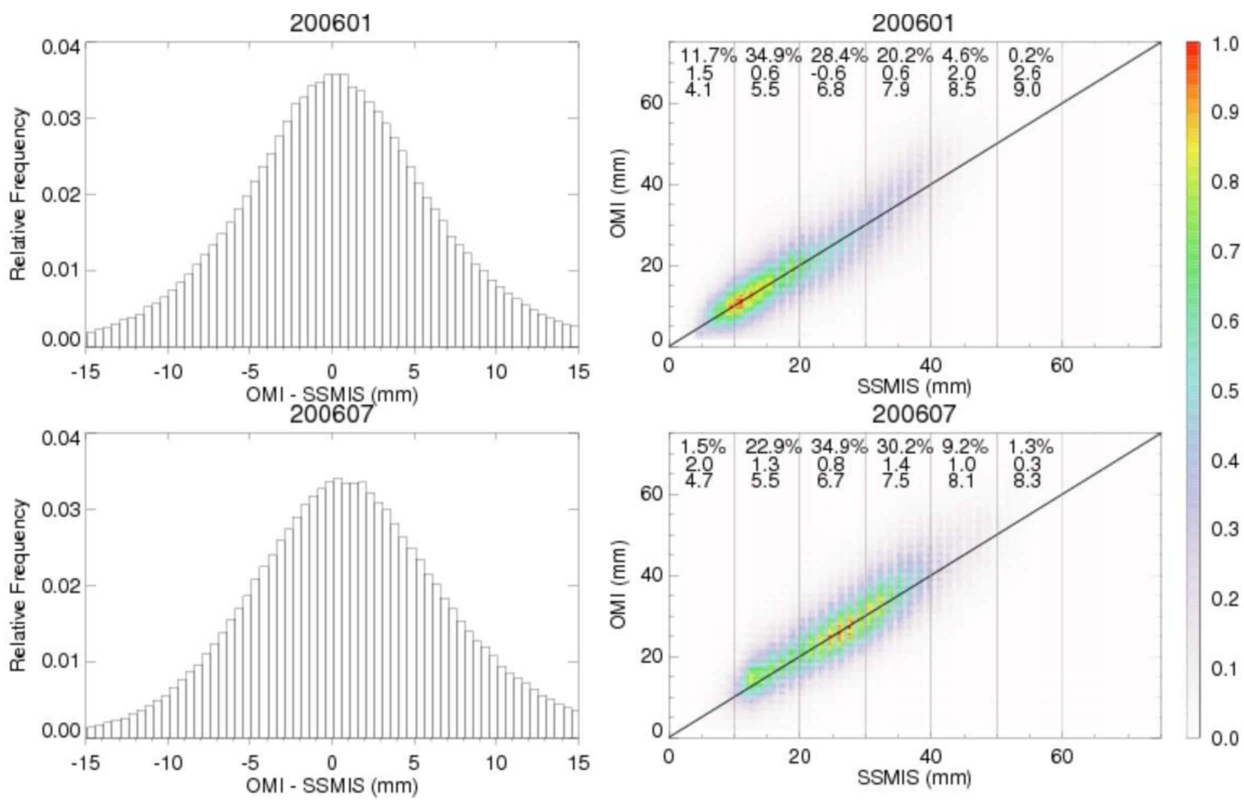

Figure 6. Comparisons between Version 4.0 OMI and SSMIS over the oceans for (top) January 2006 and (bottom) July 2006. Panels in the left column show the relative occurrence frequency of OMI-SSMIS (mm). Panels in the right column show the normalized joint distribution of SSMIS versus OMI TCWV (mm).

The left column of Figure 6 shows the distribution of OMI-SSMIS for January and July 2006. For July, the mean of OMI-SSMIS is 1.1 mm with a standard deviation of 6.8 mm, the mean absolute error |OMI-SSMIS| is 5.2 mm; for January, the mean error, standard deviation and mean absolute error are 0.4 mm, 6.5 mm and 5.0 mm, respectively. This suggests a slightly better agreement for January than for July. In comparison with the (OMI-GPS) over land (Section 3.1), OMI-SSMIS over the oceans has somewhat larger bias and standard deviation. However, as TCWV over the oceans are generally larger than that over land (compare Figure 6 with Figure 2), the relative bias and scatter are actually similar.

The right column of Figure 6 shows the normalized joint distribution of SSMIS versus OMI for January and July 2006. The correlation coefficients are r = 0.84 and 0.82 for January and July, respectively. For January, OMI-SSMIS remains within 0.6 mm of zero for TCWV in the 10 – 40 mm range, but is 1.5 mm for TCWV in the 0 – 10 mm range (only a small fraction of data pairs have TCWV > 40 mm); for July, OMI-GPS is 0.8 mm for the TCWV = 20 – 30 mm bin, and varies between 0.8 and 1.4 mm for TCWV in the 10 – 50 mm range (only a small fraction of data pairs have TCWV < 10 mm or > 50 mm). For TCWV bins that have > 5% of the data pairs, the standard deviation of OMI-SSMIS vary between 4.1 and 8.1 mm. Overall, Version 4.0 OMI data compare reasonably well with SSMIS data for TCWV in the 10 – 40 mm range, with the smallest bias occurring in the TCWV = 20 – 30 mm bin.

The agreement between Version 4.0 OMI with SSMIS is better than that between Version 3.0 OMI and SSMIS. For July 2006, using the same data filtering criteria as before, we find that Version 3.0 OMI – SSMIS has a mean of 3.2 mm with a standard deviation of 7.8 mm. The bias is much larger than that for Version 4.0 OMI – SSMIS. Again, this is because of the much larger SCD of Version 3.0 OMI TCWV due to the water vapor reference spectrum (Supplementary Figure 1).

Table 3 shows the effect of cloud fraction threshold (f) on the comparison between SSMIS and Version 4.0 OMI TCWV. The comparisons are performed using daily filtered Level 3 data for July 2006. For SSMIS, we only filter out pixels affected by rain. To investigate the influence of clouds, cloud liquid water is not used to filter the SSMIS data here. This is less restrictive than the criteria used for Figure 6 as the SSMIS pixels with cloud liquid water are filtered out in Figure 6 for the "clear-sky" comparison there. For OMI, we require MDQFL = 0, RMS < 0.001, 0 < TCWV < 75 mm, cloud top pressure > 750 mb and cloud fraction < f. Results show that OMI is higher than SSMIS by 0.02 – 3.07 mm for f = 0.05 – 0.45. The difference between the f = 0.05 case of Table 3 and the f = 0.05 case of Figure 6 is due to the relaxed SSMIS filtering criteria. The closest agreement in terms of the mean and standard deviation of OMI-SSMIS occurs when f = 0.05. The number of SSMIS and OMI data pairs more than doubles between f = 0.05 and f = 0.15. The linear correlation coefficient varies between 0.82 and 0.85 within the range of f values considered. The best linear regression line (OMI = 0.70 + 1.02 * SSMIS) occurs when f = 0.15. Therefore, for OMI over the oceans, we recommend using cloud fraction threshold f = 0.05 – 0.15, in combination with the other usual data filtering criteria, though users are advised to make their own decisions based on their tolerance and applications.

Table 3. Effect of cloud fraction threshold on the comparison between SSMIS and Version 4.0 OMI TCWV for July 2006. f: OMI cloud fraction threshold; N: number of qualifying data pairs; P: Percentage of qualifying data pairs with respect to the total number of qualifying SSMIS data points; Mean: mean of OMI-SSMIS in mm; σ: standard deviation of OMI-SSMIS in mm; MAE: Mean absolute error |OMI-SSMIS| in mm; r: correlation coefficient between SSMIS and OMI; R^2: coefficient of determination for linear regression OMI = b + k * SSMIS, where OMI and SSMIS are in mm; b: Intercept of linear regression; k: slope of linear regression.

f	N	P (%)	Mean	σ	MAE	r	R^2	b	k
0.05	1,048,879	7.4	0.02	7.11	5.39	0.82	0.67	1.43	0.95
0.15	2,837,032	20.0	1.38	7.82	5.84	0.84	0.71	0.70	1.02
0.25	3,932,468	27.8	2.20	8.09	6.09	0.84	0.71	1.11	1.04
0.35	4,819,185	34.0	2.73	8.22	6.24	0.85	0.72	1.45	1.05
0.45	5,537,003	39.1	3.07	8.26	6.32	0.85	0.72	1.62	1.06

Lowering the value for cloud top pressure threshold also leads to larger bias and scatter. For example, when cloud fraction threshold f = 0.05 and cloud top pressure > 500 mb are used, the mean and standard deviation of OMI-SSMIS become 0.80 mm and 7.9 mm, both are larger than those for f = 0.05 in Table 3, though the linear regression line improves to OMI = 0.63 + 1.01 * RSS due to an increase in the dynamical range of TCWV. It should be noted that the OMCLDO2 cloud product shows good agreement with ground-based observations for clouds at altitudes lower than 2.5 km where single cloud layers dominate, but shows significant bias and large scatter for clouds at altitudes higher than 2.5 km where multi-layer clouds dominate (Veefkind et al., 2016). Thus, OMI TCWV data corresponding to low cloud top pressure (high altitude) should be used with caution. Relaxing the filtering criteria for both cloud fraction and cloud top pressure will lead to larger bias and scatter, therefore, it is not recommended. As an example, for cloud fraction < 0.15 and cloud top pressure > 300 mb, the mean (standard deviation) of OMI-SSMIS becomes 2.8 mm (9.0 mm) for July 2006.

4 Applications

4.1 El Niño / La Niña

In Figure 7, we examine the signals associated with El Niño and La Niña in Version 4.0 OMI TCWV. Panel (a) shows the Multivariate ENSO Index (MEI) from NOAA (Wolter and Timlin, 1998) (https://www.esrl.noaa.gov/psd/enso/mei/). Positive (negative) values correspond to El Niño (La Niña) conditions. We examine the anomalies in TCWV for July 2010 (MEI = -1.103, La Niña) and July 2015 (MEI = 1.981, El Niño) in the bottom row. Although these events are strong within the OMI record (from 2005 to the present), they are mild in comparison with the extrema. Between 1950 and 2018, the maximum MEI is 3.008 (in March 1983) and the minimum MEI is -2.247 (in June 1955).

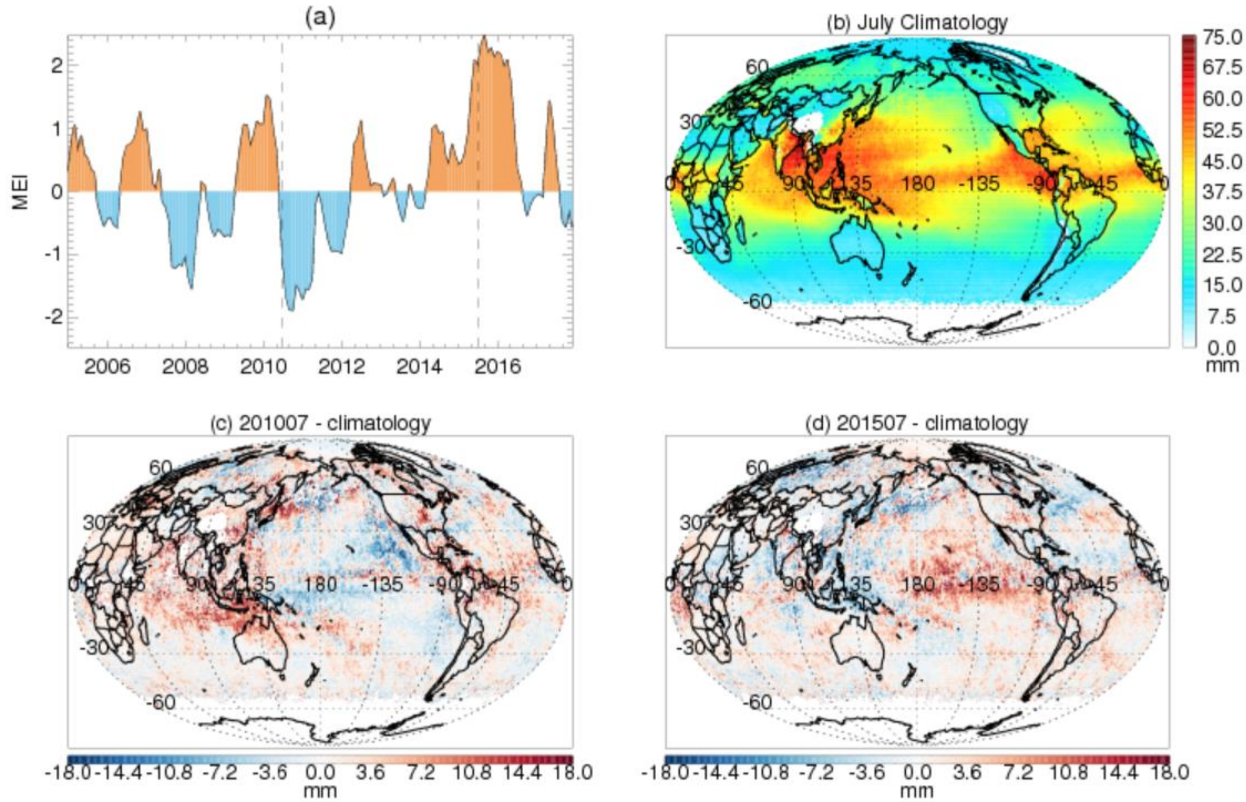

Figure 7. Top row: (a) Multivariate ENSO Index. Dashed vertical lines indicate July 2010 and July 2015; (b) TCWV (mm) climatology for July derived from Version 4.0 OMI data. Bottom row: TCWV anomaly (mm) with respect to the climatology for (c) July 2010 and (d) July 2015.

To examine the changes in OMI TCWV under different conditions, we first generate the monthly Level 3 (0.5°×0.5°) OMI TCWV using the Level 2 data for July 2005 and July 2015 using the method described in Section 3.2 (with a cloud fraction threshold of f = 0.15 and a cloud top pressure threshold of 750 mb). Then, using the same data filtering criteria, we derive the climatology for July using all the Level 2 July data between 2005 and 2015 (Figure 7b). Finally, we plot the deviations from the climatology (mm) for July 2010 and July 2015 in Figure 7(c) and 7(d), respectively.

The TCWV anomalies exhibit large-scale patterns. The pattern for July 2015 largely opposes that for July 2010. Particularly, in July 2015 under El Niño conditions, TCWV are higher in the equatorial central and eastern Pacific and lower in the Indonesia region; while in July 2010 under La Niña conditions, TCWV are lower in the tropical eastern Pacific and equatorial western

Pacific and higher in Indonesia and the Indian Ocean. The overall patterns largely conform to the results derived from the Hamburg Ocean Atmosphere Parameters and Fluxes from Satellite Data (HOAPS) data (Shi et al., 2018).

4.2 Corn Sweat

"Corn sweat" refers to a hot and humid condition associated with heat waves which results in large evapotranspiration rate in the Midwestern United States where cropland is often the dominant land usage type. Besides evaporation, transpiration by plants, such as corn, draws water from the soil to the atmosphere, enhancing the humidity and increasing the heat index. A corn sweat event from July 18 to July 24 in 2016 made news in the US. This event is examined in Figure 8 using the Version 4.0 OMI TCWV.

Figure 8 (a) and 8(b) show the Level 3 (0.25°×0.25°) OMI TCWV for July 18 - July 24 (7-day) and June 1 – August 31 (JJA) in 2016, respectively. The 7-day period corresponds to the corn sweat event. The 0.25°×0.25° Level 3 data are derived using the same filtering criteria as those used for Figure 7. Figure 8(c) indicates the anomaly associated with the corn sweat event relative to the JJA mean. High TCWV is observed for the 7-day period from the Gulf coast to the Midwestern US. Besides the Gulf region, the largest TCWV enhancements (of up to 18+ mm) occur in parts of Iowa (IA), Missouri (MO), Illinois (IL) and Indiana (IN). Elevated TCWV is also observed by several GPS stations in the general area during the same time period, though coincident OMI data are not found at the stations (Supplementary Figure 3). At a few GPS stations, high TCWV persisted a couple more days after July 24 which is most likely related to a change in the weather. As shown by the surface pressure observations at the GPS stations, the Midwest is under the control of a high-pressure system during the corn sweat period and a low-pressure system afterwards (Supplementary Figure 4).

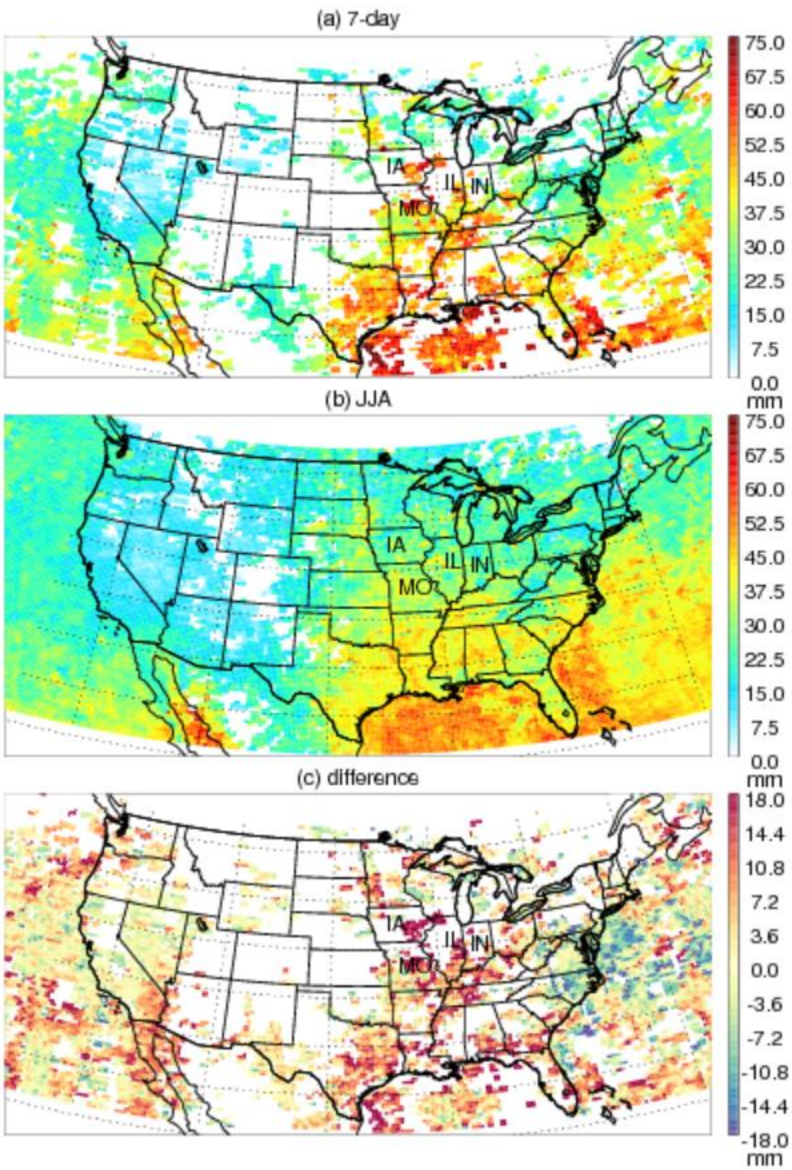

Figure 8. Level 3 (0.25°×0.25°) OMI TCWV (mm) generated using the Level 2 data during (a) July 18 - July 24, 2016 and (b) June 1 - August 31, 2016. (c) The difference of (a) - (b) in mm. The abbreviations for the states most affected by the event are indicated in the map.

To assess the significance of evapotranspiration for the Midwestern US during the corn sweat event, we carried out a sensitivity study using the Weather Research and Forecasting (WRF) model v3.9.1 (Skamarock et al., 2008). The model was run on a 36-km parent domain and a 12-km nested domain, covering the relevant areas of the US. The physics parameterizations included the WRF Single-Moment (WSM) 6-Class Microphysics (Hong and Lim, 2006), the Kain-Fritsch (KF) subgrid cumulus parameterization (Kain, 2004), the Yonsei University (YSU) planetary boundary layer scheme (Hong et al., 2006), the Noah Land-Surface Model (Ek et al., 2003; Chen and Dudhia, 2001), and the Rapid Radiative Transfer Model (RRTM). Horizontal turbulent diffusion was based on the standard Smagorinsky first-order closure. The initial and lateral boundary conditions were from the 3-hourly NCEP North American Regional Reanalysis (NARR) at 32-km resolution. To reduce the uncertainty associated with lateral boundary condition for the nested domain, we nudged the model in the parent domain toward the reanalysis, but left the nested domain running freely.

To diagnose the contribution of evapotranspiration, the model was run from July 19th to July 22nd of 2016 with and without evapotranspiration (calculated in the Noah Land-Surface model). The results for July 21st are shown in Figure 9. TCWV is generally lower in the interior of the domain for the run without evapotranspiration (No ET). The higher TCWV in the No ET run near the southern boundary reflects non-linear water vapor transport from the Gulf region. Turning off evapotranspiration not only directly affects the water vapor flux from the surface but also indirectly influences other meteorological variables, such as winds. Thus, there is a difference in the water vapor flux across the domain boundary. The difference between the default and No ET runs in Figure 9 suggests that evapotranspiration contributes about 15 – 25% of the TCWV in the Midwestern US during the corn sweat event. A detailed study incorporating TCWV data with the WRF model will be carried out in future work.

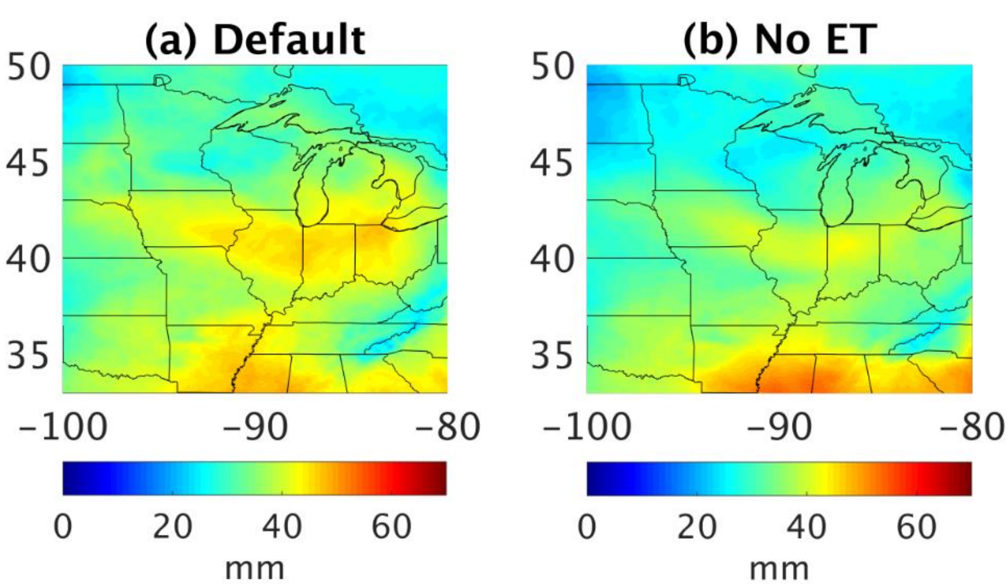

Figure 9. WRF simulations of TCWV (mm) for Midwestern US on 07/21/2016 for the run (a) with and (b) without evapotranspiration.

4.3 Atmospheric River (AR)

4.3.1 An Intense AR in OMI data

ARs are narrow elongated bands with high TCWV in the atmosphere. With flow rates similar to those of large rivers, ARs are highly important in the global hydrological cycle (Zhu and Newell, 1998). Land-falling ARs can lead to heavy orographic precipitation that affects areas such as the west coast of North America and Europe (Gimeno et al., 2014; Neiman et al., 2008b).

The extreme AR of November 6th – 7th, 2006 brought devastating flood to the Pacific Northwest – the region in western North America bounded by the Pacific to the west and the Cascade mountain range to the east. This AR is described in detail in Neiman et al., 2008a. The signature of this AR is captured in the Version 4.0 OMI TCWV data. The left column of Figure 10 shows the Level 3 OMI TCWV and its anomaly on November 6th, 2006. The Level 3 data are generated following the same procedure as that used for Figure 8. Although many pixels are missing because of the cloud filtering (cloud top pressure > 750 mb, cloud fraction < 0.15) and other criteria, the leading edge of the AR is noticeable as an elongated band of high TCWV (15+ mm above the climatology) extending from Hawaii to Northern California (indicated by arrows in Figure 7(b) and 7(c)). The position of the AR in OMI TCWV agrees well with that in Special Sensor Microwave/Imager (SSM/I) microwave observation (Neiman et al., 2008a).

The right column of Figure 10 shows the Level 3 OMI ozone mixing ratio interpolated to 200 mb and its anomaly. The OMI ozone data are retrieved using the SAO ozone profile algorithm (Liu et al., 2010; Huang et al., 2017, 2018). The climatology is derived by averaging all monthly Level 3 data for November from 2004 to 2017. The global distribution of ozone at 200 mb shows low mixing ratio in the low latitudes and high mixing ratio in the high latitudes, opposite to the global distribution of TCWV. The anomaly shows a curvilinear band of high ozone that is parallel to the AR in the left column, but is located further to the west. This feature indicates intrusion of ozone rich stratospheric air along the polar front, and is associated with the same extra-tropical cyclone as the AR is.

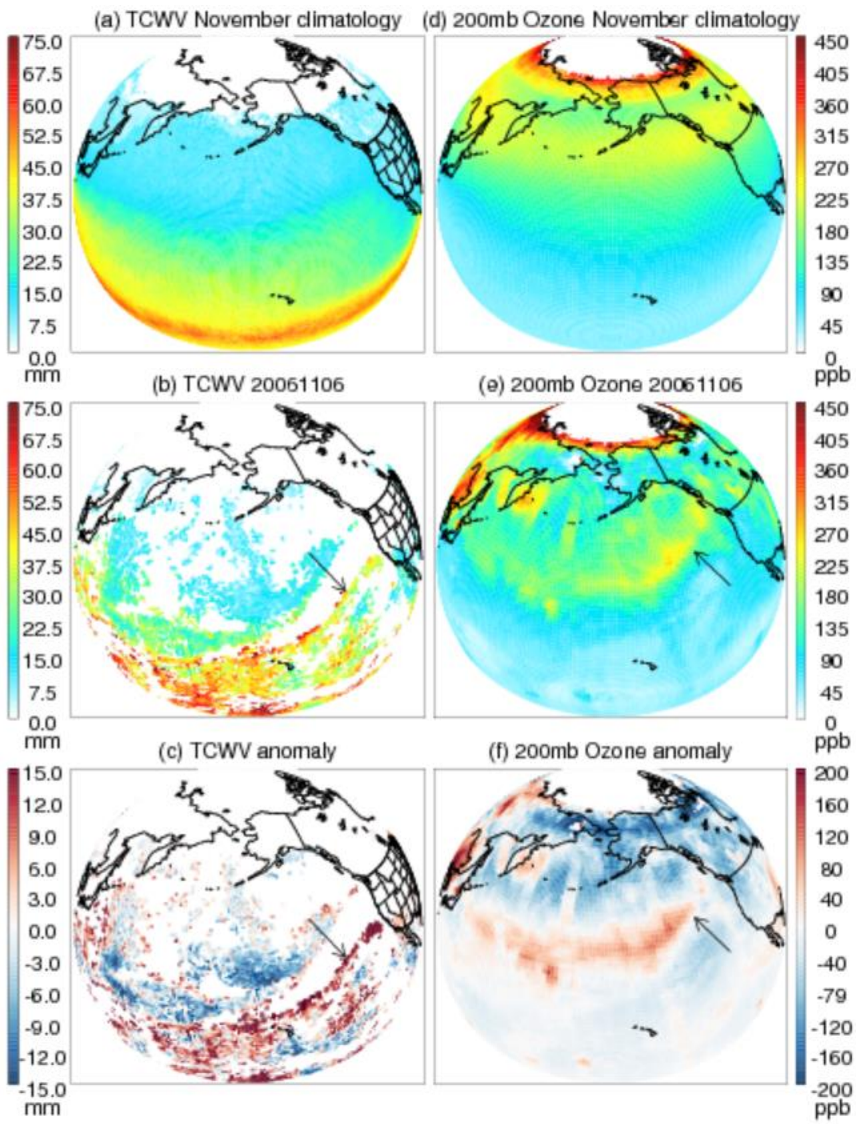

Figure 10. The Level 3 (top row) climatology, (middle row) data on November 6th, 2006 and (bottom row) anomaly on November 6th, 2006 with respect to the climatology for (left column) Version 4.0 OMI TCWV (mm, 0.5°×0.5°) and (right column) OMI ozone mixing ratio (ppb, 1°×1°) interpolated to 200 mb.

4.3.2 OMI TCWV Assimilation for the AR

To evaluate the potential of OMI water vapor data to improve numerical weather forecasts, we conducted a data assimilation experiment from November 2nd to November 8th of 2006 using WRF v3.9.1 and Version 4.0 OMI TCWV. The model was configured with a 27-km (290×270 surface grid points with 51 vertical levels), a 9-km (586×586×51 points) and a 3-km (541×526×51) nested domains in a Lambert projection over the relevant portion of the Pacific and North America (Figure 11 top left). The domains are designed for the November 6 AR event and its associated precipitation at landfall. The model has the same physics parameterizations as those used in Section 4.2 except that a more sophisticated double-moment microphysics scheme is used for quantifying precipitation. The initial and boundary conditions for the 27-km domain were from the 1°×1° NCEP FNL reanalysis. One-way nesting is used for the inner domains. To evaluate the model's skill at simulating the AR and the contribution of OMI TCWV to the quality of the simulation, we did not nudge the run towards the reanalysis, nor assimilate the observed sea surface temperature within the computational domains.

The OMI TCWV is assimilated into the model using analytical optimal estimation (Rodgers, 2000). This method minimizes the cost function $J(\boldsymbol{x}) = (\mathbf{y} - H\boldsymbol{x})^T\mathbf{E}^{-1}(\mathbf{y} - H\boldsymbol{x}) + (\boldsymbol{x} - \boldsymbol{x}^b)^T\mathbf{B}^{-1}(\boldsymbol{x} - \boldsymbol{x}^b)$, where x is the true TCWV, x^b is the a priori TCWV (from the model), y is the observed TCWV, H represents the model Jacobian, **B** and **E** are the error covariance matrices of the a priori and observation. **B** is estimated using the 12-hour and 24-hour forecasts using the National Meteorological Center method (Parrish and Derber, 1992). **E** is based on the fitting uncertainties of OMI data.

The a posteriori analysis ($\hat{\boldsymbol{x}}$) can be obtained from $\hat{\boldsymbol{x}} = \boldsymbol{x}^b + \mathbf{K}(\mathbf{y} - H\mathbf{x})$, where $\mathbf{K} = \mathbf{B}H^T(H\mathbf{B}H^T + W^{-1}\mathbf{E})^{-1}$ is the Kalman gain, $W = \frac{(R^2-r^2)}{(R^2+r^2)}$ is the Cressman function to weigh the observations based on their Euclidian distance r to the model grids, and R is the influence radius of the observations. We simply assume R to be 1°, 0.5° and 0.25° for the 27-km, 9-km and 3-km domain to get a quick look at the results in this paper and leave a more vigorous quantification of R to future work. The a posteriori TCWV is solved hourly when OMI data are available and is used to initialize the next simulation window.

During the assimilation, we adjust the OMI data using the AMF calculated with the modeled water vapor profile ($OMI_{satellite}^{adjusted} = \frac{OMI_{satellite} \times AMF_{satellite}}{AMF_{model}}$) and the scattering weights provided with the Level 2 OMI data. This can reduce the observational error associated with using the monthly mean water vapor profile in the operational OMI product. The standard deviation of the difference between $AMF_{satellite}$ and AMF_{model} is about 20%.

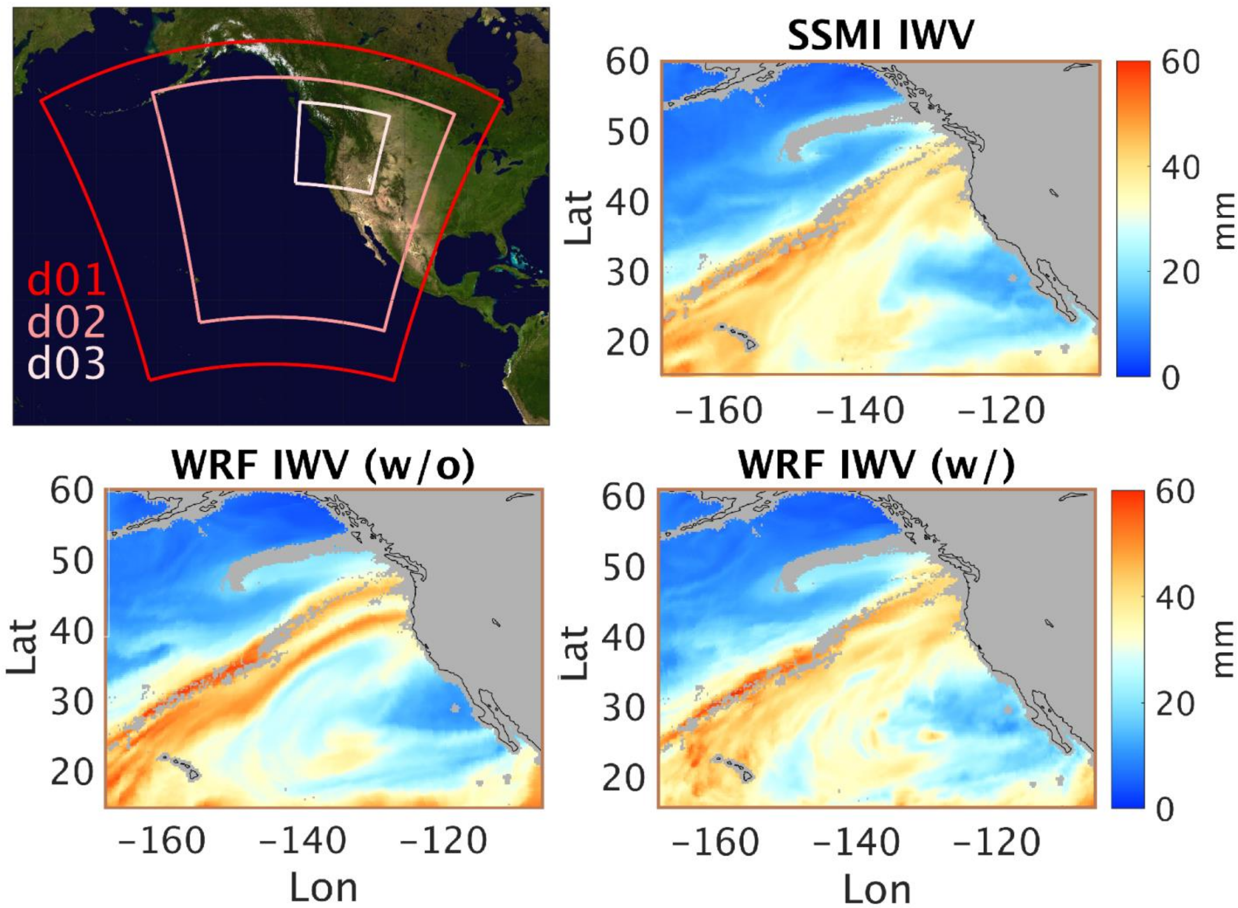

Figure 11. Top left: WRF model domain configuration for the November 2006 AR event. Top right: TCWV observed by SSM/I on November 6th, 2006. Bottom row: TCWV simulated by WRF on the same day (left) without and (right) with OMI TCWV data assimilation. Gray color indicates area with no SSM/I data.

Figure 11 shows the zoomed-in views of the AR on November 6th, 2006. The TCWV independently observed by SSM/I is shown in the upper right panel. The lower left and lower right panels show the model results without and with OMI TCWV assimilation. The model without assimilation shows an AR that is split into two parallel filaments making landfall at separate locations on the west coast of North America, where the TCWV is too high compared to the SSM/I observation, especially for the southern filament. As discussed later, this has a significant impact on precipitation (Figure 12). After assimilating OMI TCWV, the modeled

TCWV agrees much better with the SSM/I observation. The spurious southern filament disappeared, the overall shape and amplitude of the AR are significantly improved.

The location and intensity of precipitation over land are crucial for local flood control and water resource management, and are closely related to the shape and strength of AR at landfall. The 24-hour accumulated precipitation on November 6 in the 3-km domain is examined in Figure 12. The model output is coarsened to 0.25°×0.25° to match the resolution of the Tropical Rainfall Measuring Mission (TRMM) observation product. The model without OMI data assimilation produces spurious rainfall over the Oregon - California border (box A) as a result of the erroneously strong southern filament of the simulated AR (Figure 11, lower left panel). This artifact was removed after OMI data assimilation, showing better agreement with the corresponding TRMM rainfall observation. The difference in rainfall between the assimilation and observation in the Oregon / Washington area is probably related to both the model error and the data error, as well as the data density and distribution. A detailed error attribution for precipitation is beyond the scope of this paper.

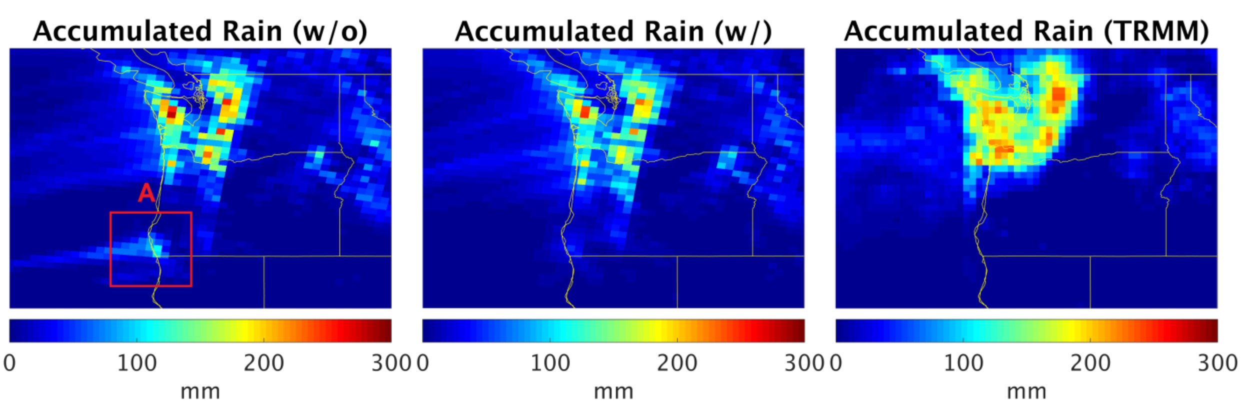

Figure 12. The simulated rainfall accumulated from 0000 UTC to 2300 UTC (in mm) on November 6, 2006 for the model (left) without and (middle) with OMI TCWV assimilation. The rightmost panel show the accumulated rainfall observed by TRMM for the same time period. Note that the 3-km model result is coarsened to match the resolution of the TRMM product. Box A highlights the erroneously simulated precipitation in the run without OMI TCWV data assimilation.

5 Summary and Conclusion

The Version 4.0 retrieval algorithm for OMI Total Column Water Vapor (TCWV) is presented in this paper. The algorithm follows the usual two-step approach where Slant Column Density (SCD) is derived from spectral fitting and Vertical Column Density (VCD) is obtained through the ratio of SCD and Air Mass Factor (AMF). In Version 4.0, the spectral fitting no longer considers common mode. The retrieval window (432.0 - 466.5 nm) results from a systematic optimization that reflects trade-offs among several factors, including small fitting RMS, small fitting uncertainty, large fraction of successful retrieval and long retrieval window length. The AMF calculation uses the latest OMI O_2-O_2 cloud product (Veefkind et al., 2016) and monthly variable vertical profiles from the MERRA-2 reanalysis (Gelaro et al., 2017).

The Version 4.0 OMI TCWV product is compared against the GPS network data over land and the SSMIS microwave observations over the oceans for 2006. Version 4.0 OMI TCWV has much smaller bias than Version 3.0 and has replaced previous versions on the Aura Validation Data Center website. Version 4.0 OMI TCWV is characterized under different cloud conditions. Under “clear-sky” condition (cloud fraction < 5% and cloud top pressure > 750 mb), the overall mean of OMI-GPS over land is 0.32 mm with a standard deviation of 5.2 mm, and the smallest bias occurs when TCWV is between 10 mm and 20 mm; the overall mean of OMI-SSMIS over the oceans is 0.4 – 1.1 mm with a standard deviation of 6.5 - 6.8 mm, and the smallest bias occurs for TCWV between 20 mm and 30 mm. The correlation coefficient between OMI TCWV and the reference datasets realizes the largest gain when the cloud fraction threshold is increased from 5% to 15%. The regression line appears the best when f = 0.25 is used over land and when f = 0.15 is used over the oceans. But, larger cloud fraction leads to larger bias and scatter. Thus, for most applications, we recommend to consider only OMI data with cloud fraction < 5% to 25% and cloud top pressure > 750 mb, in addition to main data quality flag = 0, no row anomaly, fitting RMS < 0.001 and 0<TCWV<75 mm. Relaxing the cloud top pressure threshold has a similar effect as relaxing the cloud fraction threshold. TCWV corresponding to low cloud top pressure (high altitude) should be used with caution due to the degraded accuracy for these clouds in the OMCLDO2 product.

As example applications of the Version 4.0 OMI TCWV data across a variety of temporal and spatial scales, this paper examines the climate pattern associated with El Niño / La Niña, the enhanced humidity during a week-long corn sweat event in the Midwest US, and the linear band of high TCWV associated with an intense atmospheric river which made landfall on the west coast of North America. Strong signals are found in OMI TCWV for all three examples. A data assimilation experiment shows that the OMI TCWV data can help improve WRF's skill of simulating the shape and intensity of the AR, as well as the accumulated rainfall near the coast.

Further improvement of the product can proceed from both spectral fitting and AMF calculation, such as, water vapor reference spectrum, instrument slit-function and solar irradiance for spectral fitting, aerosol correction and surface bi-directional reflectance for AMF calculation.

Data availability

The GPS network data are downloaded from NCAR (rda.ucar.edu/datasets/ds721.1). The SSMIS data used in this paper are downloaded from the Remote Sensing Systems (http://www.remss.com/support/data-shortcut/). The Multivariate ENSO Indices are downloaded from NOAA (https://www.esrl.noaa.gov/psd/enso/mei/table.html). OMI TCWV and ozone profile data are released through the Aura Validation Data Center (https://avdc.gsfc.nasa.gov/).

Author contribution

Huiqun Wang optimized the OMI TCWV retrieval window, performed the data validation and tested most of the data application described in this paper. Amir Souri performed the WRF simulations and data assimilation experiment presented in this paper. Gonzalo González Abad improved and maintained the SAO retrieval code and implemented OMI TCWV data production for the Aura Validation Data Center. Xiong Liu developed the OMI ozone profile retrieval and provided the relevant data used in the AR application. Kelly Chance is the PI of the NASA grant, and is responsible for the overall direction and execution of the project. Huiqun Wang prepared and revised the manuscript with contributions from all co-authors. All authors contributed to technical and scientific discussions during this project.

Competing interests

The authors declare that they have no conflict of interest.

Acknowledgement

We thank NASA's ACMAP program (Grant NNX17AH47G) for support.

References

Brion, J., Chakir, A., Daumont, D., Malicet, J. and Parisse, C.: High-resolution laboratory absorption cross section of O3 - temperature effect, Chem. Phys. Lett., 213 (5-6), 610-612, doi:10.1016/0009-2614(93)89169-1, 1993.

Chance, K. and Spurr, R. J. D.:, Ring effect studies: Rayleigh scattering, including molecular parameters for rotational Raman scattering, and the Fraunhofer spectrum, Applied optics, 36, No. 21, 5224-5230, 1997.

Chance, K., Kurosu, T. P., Sioris, C. E.:, Undersampling correction for array detector-based satellite spectrometers. Appl. Opt., 44, 1296-1304, doi:10.1364/AO.44.001296, 2005.

Chen, F. and J. Dudhia: Coupling an Advanced Land Surface-Hydrology Model with the Penn State-NCAR MM5 Modeling System. Part I: Model Implementation and Sensitivity. Mon. Wea. Rev., 129, 569-585, 2001.

Dee, D. P., Uppala, S. M., Simmons, A. J., Berrisford, P., Poli, P., et al.: The ERA-Intrim reanalysis: configuration and performance of the data assimilation system, Q. J. R. Meteorol. Soc., 137, 553-597, 2011.

Diedrich. H., Wittchen, F., Preusker, R., and Fischer, J.: Representativeness of total column water vapour retrievals from instruments on polar orbiting satellites, Atmos. Chem. Phys., 16, 8331-8339, doi:10.5194/acp-16-8331-2016, 2016.

Dobber, M., Voors, R., Dirksen, R., Kleipool, Q. and Levelt, P.: The high-resolution solar reference spectrum between 250 and 550 nm and its application to measurements with the Ozone Monitoring Instrument, Solar Physics, 249, 2, 281-291, doi:10.1007/s11207-008-9187-7, 2008.

Ek, M. B., Mitchell, K. E., Lin, Y., Rogers, E., Grunmann, P., Koren, V., et al.: Implementation of Noah land surface model advances in the National Centers for Environmental Prediction operational mesoscale Eta model. *Journal of Geophysical Research: Atmospheres*, *108*(D22), 2003.

Gelaro, R., McCarty, W., Suarez, M. J., Todling, R., Molod, A., et al.: The Modern-Era retrospective analysis for research and applications, Version 2 (MERRA-2), J. Climate, 30, 5419-5454, doi:10.1175/JCI-D-16-0758.1, 2017

Gimeno, L., Nieto, R., Vazquez, M. and Lavers, D. A.: Atmospheric rivers: a mini-review, Frontiers in Earth Sci., 2, Art. 2, doi:10.3389/feart.2014.00002, 2014.

González Abad, G., Liu, X., Chance, K., Wang, H., Kurosu, T. P. and Suleiman, R.: Updated Smithsonian Astrophysical Observatory Ozone Monitoring Instrument (SAO OMI) formaldehyde retrieval, Atmos. Meas. Tech., 8, 19-32, doi:10.5194/amt-8-19-2015, 2015.

Hong, S. Y. and Lim, J. O. J.: The WRF single-moment 6-class microphysics scheme (WSM6). *J. Korean Meteor. Soc*, *42*(2), 129-151, 2006.

Hong, S. Y., Noh, Y. and Dudhia, J.: A new vertical diffusion package with an explicit treatment of entrainment processes. *Monthly weather review*, *134*(9), 2318-2341, 2006.

Huang, G., Liu, X., Chance, K., Yang, K., Bhartia, P. K., Cai, Z., Allaart, M., Ancellet, G., Calpini, B., Coetzee, G. J. R., et al.: Validation of 10-year SAO OMI ozone profile (PROFOZ) product using ozonesonde observations, Atmos. Meas. Tech., 10, 7, doi:10.5194/amt-10-255-2017, 2017.

Huang, G., Liu, X., Chance, K., Yang, K., Cai, Z.: Validation of 10-year SAO OMI ozone profile (PROFOZ) product using Aura MLS measurements, Atmos. Meas. Tech., 11, 1, 17-32, doi:10.5194/amt-11-17-2018, 2018.

Kain, J.S.: The Kain–Fritsch convective parameterization: an update. *Journal of applied meteorology*, *43*(1), 170-181, 2004.

Kleipool, Q. L., Dobber, M. R., de Hann, J. F., and Levelt, P. F.: Earth surface reflectance climatology from 3 years of OMI data, J. Geophys. Res., 113, D18308, doi:10.1029/2008JD010290, 2008.

Lampel, J., Frieß, and Platt, U.: The impact of vibrational Raman scattering of air on DOAS measurements of atmospheric trace gases, Atmos. Meas. Tech., 8, 3767-3787, doi:10.5194/amt-8-3767-2015, 2015a.

Lampel, J., Pohler, D., Tschritter, J., Friess, U., Platt, U.: On the relative absorption strengths of water vapour in the blue wavelength range, Atmos. Meas. Tech., 8, 4329-4346, doi:10.5194/amt-8-4329-2015, 2015b.

Liu, X., Bhartia, P. K., Chance, K., Spurr, R. J. D., Kurosu, T. P.: Ozone profile retrievals from the Ozone Monitoring Instrument, Atmos. Chem. Phys., 10, 2521-2537, doi:10.5194/acp-10-2521-2010, 2010.

Lorente, A., Boersma, K. F., Yu, H., Dorner, S., Hillboll, A., Richter, A., Liu, M., Lamsal, L. N., Barkley, M., De Smedt, I., Van Roozendael, M., Wang, Y., Wagner, T., Beirle, S., Lin, J., Krotkov, N., Stammes, P., Wang, P., Eskes, H. J. and Krol, M.: Structural uncertainty in air mass factor calculation for NO2 and HCHO satellite retrievals, Atmos. Meas. Tech., 10, 759-782, doi:10.5194/amt-10-759-2017, 2017.

Levelt, P. F., van den Oord, G. H., Dobber, M. R., Malkki, A., Visser, H., de Vries, J., Stammes, P., Lundell, J. O. and Saari, H.: The ozone monitoring instrument, T. Geosci. Remote, 44, 1093-1101, 2006.

Mason, J. D., Cone, M. T. and Fry, E. S.: Ultraviolet (250-550 nm) absorption spectrum of pure water, Applied optics, 55, No. 25, 7163-7172, doi:10.1364/AO.55.007163, 2016

Mears, C. A., Wang, J., Smith, D. and Wentz, F. J.: Intercomparison of total precipitable water measurements made by satellite-borne microwave radiometers and ground-based GPS instruments, J. Geophys. Res. Atmos., 120, 2492-2504, doi:10.1002/2014JD022694, 2015.

Neiman, P. J., Ralph, F. M., Wick, G. A., Kuo, Y., Wee, T., Ma, Z., Taylor, G. H., Dettinger, M. D.: Diagnosis of an intense atmospheric river impacting the Pacific northwest: storm summary and offshore vertical structure observed with COSMIC satellite retrievals, Monthly Wea. Rev., 136, 4398 – 4420, doi:10.1175/2008MWR2550.1, 2008a.

Neiman, P. J., Ralph, F. M., Wick, G. A., Lundquist, J. D., Dettinger, M. D.: Meteorological characteristics and overland precipitation impacts of atmospheric rivers affecting the West Coast of North America based on eight years of SSM/I satellite observations, J. Hydrometeorology, 9, 22-47, doi:10.1175/2007JHM855.1, 2008b.

Ning, T., Wang, J., Elgered, G., Dick, G., Wickert, J., Bradke, M., Sommer, M., Querel, R. and Smale, D.: The uncertainty of the atmospheric integrated water vapour estimated from GNSS observations, Atmos. Meas. Tech., 9, 79-92, doi:10.5194/amt-9-79-2016, 2016.

Noël, S., Buchwitz, M., Bovensmann, H., Hoogen, R., and Burrows, J. P.: Atmospheric Water Vapor Amounts Retrievd from GOME Satellite data, Geophys. Res. Lett., 26, 1841–1844, 1999.

Rodgers, C. D.: Inverse methods for atmospheric sounding, theory and practice, Series on Atmospheric, Ocean and Planetary Physics – Vol. 2, Editor: Taylor, F. W., Published by World Scientific Publishing Co. Pte. Ltd., Singapore, 2000.

Schröder, M., Lockhoff, M., Shi, L., August, T., Bennartz, R., et al.: The GEWEX Water Vapor Assessment: Overview and introduction to results and recommendations, Remote Sensing, 11, 3, doi:10.3390/rs11030251, 2019.

Skamarock W. C. and Klemp, J. B.: A time-split nonhydrostatic atmospheric model for weather research and forecasting applications, J. Computational Physics, 227, 2, 3465-3485, doi:10.1016/j.jcp.2007.01.037, 2008.

Palmer, P. I., Jacob, D. J., Chance, K., Martin, R. V., Spurr, R. J. D., Kurosu., T. P., Bey, I., Rantosca, R., Fiore, A. and Li, Q.: Air mass factor formulation for spectroscopic measurements from satellites: Application to formaldehyde retrievals from the Global Ozone Monitoring Experiment, J. Geophys. Res., 106, D13, 14539-14550, 2001.

Ralph, F. M., Neiman, P. J. and Wick, G. A.: Satellite and CALJET aircraft observations of atmospheric rivers over the eastern north Pacific ocean during the winter of 1997/98, Monthly Wea. Rev., 132, 1721-1745, doi:10.1175/1520-0493(2004)132<1721:SACAOO>2.0.CO;2, 2004.

Rothman, L. S., Gordon, I. E., Barbe, A., Benner, D. C., Bernath, P. F., et al.: The HITAN 2008 molecular spectroscopic database, J. Quant. Spectr. Radiat. Tran., 110, 533-572, 2009.

Schmidt, G. A., Ruedy, R. A., Miller, R. L. and Lacis, A. A.: Attribution of the present-day total greenhouse effect, J. Geophys. Res., 115, D20106, doi:10.1029/2010JD014287, 2010.

Schroder, M., Lockhoff, M., Fell, F., Forsythe, J., Trent, T., Bennartz, R., Borbas, E., Bosilovich, M. G., Castelli, E., Hersbach, H., Kachi, M., Kobayashi, S., Kursinski, E. R., Loyola, D., Mears, C., Preusker, R., Rossow, W. B. and Saha, S.: The GEWEX water vapor assessment archive of water vapour products from satellite observations and reanalyses, Earth Syst. Sci. Data, 10, 1093-1117, doi:10.5194/essd-10-1093-2018, 2018.

Shi, L., Schreck, C. J. III, and Schroder, M.: Assessing the pattern differences between satellite-observed upper tropospheric humidity and total column water vapor during major El Niño events, Remote Sens., 10, 1188, doi:10.3390/rs10081188, 2018.

Spietz, P., Martin, J. C. G. and Burrows, J. P.: Spectroscopic studies of the I-2/O-3 photochemistry – Part 2. Improved spectra of iodine oxides and analysis of the IO absorption spectrum, J. Photochemistry and Photobiology, 176 (1-3), 50-67, doi:10.1016/j.photochem.2005.08.023, 2005.

Thalman, R. and Volkamer, R.: Temperature dependent absorption cross-sections of O2-O2 collision pairs between 340 and 630 nm and at atmospherically relevant pressure, Phys. Chem. Chem. Phys., 15, 15371-15381, doi:10.1039/c3cp50968k, 2013.

Vandaele, A. C., Hermas, C., Simon, P. C., Carleer, M., Colin, R., Fally, S., Merienne, M. F., Jenouvier, A. and Coquart, B.: Measurements of the NO2 absorption cross-section from 42000 cm(-1) to 10000 cm(-1) (238-1000 nm) at 200 K and 294 K, J. Quant. Spectr. Radiat. Trans., 59, 171-184, doi:10.1016/S0022-4073(97)00168-4, 1998.

Vasilkov, A., Qin, W., Krotkov, N., Lamsal, L., Spurr, R., Haffner, D., Joiner, J., Yang, E. and Marchenko, S.: Accounting for the effects of surface BRDF on satellite cloud and trace-gas retrievals: a new approacj based on geometry-dependent Lambertian equivalent reflectivity applied to OMI algorithms, Atmos. Meas. Tech., 10, 333-349, doi:10.5194/amt-10-333-2017, 2017.

Veefkind, J. P., de Hann, J. F., Sneep, M. and Levelt, P. F.: Improvements to the OMI O2-O2 operational cloud algorithm and comparisons with ground-based radar-lidar observations, Atmos. Meas. Tech., 9, 6035-6049, doi:10.5194/amt-9-6035-2016, 2016.

Volkamer, R., Spietz, P., Burrows, J. and Platt, U.: High-resolution absorption cross section of glyoxal in the UV/Vis and IR spectral ranges, J. Photochem. Photobio., 172, 35-46, doi:10.1016/j.jphotochem.2004.11.011, 2005.

Wagner, T., Beirle, S., Sihler, H. and Mies, K.: A feasibility study for the retrieval of the total column precipitable water vapour from satellite observations in the blue spectral range, Atmos. Meas. Tech., 6, 2593-2605, doi:10.5194/amt-6-2593-2013, 2013.

Wang, H., Liu, X., Chance, K., González Abad, G. and Chan Miller, C.: Water vapor retrieval from OMI visible spectra, Atmos. Meas. Tech., 7, 1901-1913, doi:10.5194/amt-7-1901-2014, 2014.

Wang, H., González Abad, G., Liu, X. and Chance, K.: Validation and update of OMI total column water vapor product, Atmos. Chem. Phys., 16, 11379-11393, doi:10.5194/acp-16-11379-2016, 2016.

Wentz, F. J.: A well-calibrated ocean algorithm for special sensor microwave/imager, J. Geophys. Res., 102(C4), 8703-8718, doi:10.1029/96JC01751, 1997.

Wolter, K. and Timlin, M.S.: Measuring the strength of ENSO events - how does 1997/98 rank? Weather, 53, 315-324, 1998.

Zhu, Y. and Newell, R. E.: A proposed algorithm for moisture fluxes from atmospheric rivers, Monthly Weather Rev., 126, 3, 725-735, doi:10.1175/1520-0493(1998)126<0725:APAFMF>2.0.CO;2, 1998.